

Dust and Volatiles in the Disintegrating Comet C/2019 Y4 (ATLAS)

RUINING ZHAO ^{1,2} AIGEN LI ³ BIN YANG ⁴ LIANG WANG ^{5,6} HUIJUAN WANG ^{7,2}
YU-JUAN LIU,⁷ AND JIFENG LIU ^{7,8,2,9}

¹CAS Key Laboratory of Optical Astronomy, National Astronomical Observatories, Chinese Academy of Sciences, Beijing 100101, China; rnzhao@nao.cas.cn; jfliu@nao.cas.cn

²School of Astronomy and Space Sciences, University of Chinese Academy of Sciences, Beijing 100049, China

³Department of Physics and Astronomy, University of Missouri, Columbia, MO 65211, USA; lia@missouri.edu

⁴Instituto de Estudios Astrofísicos, Facultad de Ingeniería y Ciencias, Universidad Diego Portales, Santiago, Chile; bin.yang@mail.udp.cl

⁵Nanjing Institute of Astronomical Optics & Technology, Chinese Academy of Sciences, Nanjing 210042, China

⁶CAS Key Laboratory of Astronomical Optics & Technology, Nanjing Institute of Astronomical Optics & Technology, Chinese Academy of Sciences, Nanjing 210042, China

⁷CAS Key Laboratory of Optical Astronomy, National Astronomical Observatories, Chinese Academy of Sciences, Beijing 100101, China

⁸New Cornerstone Science Laboratory, National Astronomical Observatories, Chinese Academy of Sciences, Beijing 100012, China

⁹Institute for Frontiers in Astronomy and Astrophysics, Beijing Normal University, Beijing, 102206, China

(Received January 5, 2024; Revised January 5, 2024; Accepted January 5, 2024)

Submitted to ApJ

ABSTRACT

C/2019 Y4 (ATLAS) is an Oort cloud comet with an orbital period of ~ 5895 yr. Starting in March 2020, its nucleus underwent disintegration. In order to investigate the gas and dust properties of C/2019 Y4 (ATLAS) during its disintegration, we obtained long-slit spectra at 3600–8700 Å and *BVRI* multi-band images with the Xinglong 2.16-Meter Telescope in April 2020. Our observations revealed that C/2019 Y4 (ATLAS) exhibited strong emission bands of CN, C₂, C₃, and NH₂ which are superimposed on a dust scattering continuum, typical of cometary spectra in the optical. The production rates of CN, C₂, and C₃ derived using the Haser model and the corresponding C₂/CN and C₃/CN ratios suggest that C/2019 Y4 (ATLAS) is a “typical” Oort cloud comet under the A’Hearn classification, although it appears less dusty as revealed by the $Af\rho$ quantities. Its dust-scattering reflectivity is slightly red, with a gradient of $\sim 5\%$ per 10^3 Å. We model the reflectivity gradient in terms of porous dust and find that the red color is accounted for by porous dust.

Keywords: Long period comets (933); Comets (280); Small solar system bodies (1469)

1. INTRODUCTION

Cometary nuclei are the most primitive objects in the solar system and have preserved pristine materials from the presolar molecular cloud and from the early stages of the protosolar nebula.

Therefore, the origin of cometary nuclei is closely linked to the origin of the solar system. The chemical and physical properties of dust and volatile materials in cometary nuclei and comae shed light on the nature of the primordial interstellar materials present during the solar system formation, and provide clues to the processes of incorporation of these materials into cometary nuclei, as well as the chemical and thermodynamic conditions in the outer solar nebula in which comets formed.

In the absence of a direct analysis of cometary nucleus materials, one often resorts to cometary comae formed by volatiles outgassed from the nucleus and dust particles dragged out by the expanding gas. Once formed and stored in the Oort cloud or the Kuiper belt, however, comets are exposed for ~ 4.5 billion years to the flux of Galactic cosmic rays and may develop a substantial “crust” of non-volatile materials (e.g., see [Strazzulla 1999](#)). For short-period comets, such a crust could also result from the solar radiation during their numerous close approaches to the Sun (e.g., see [Li & Greenberg 1998a](#)). In this scenario, only the sub-surface materials still remain pristine. Therefore, disintegrating comets provide us an unique opportunity to gain access to the pristine, sub-surface materials.

Comet C/2019 Y4 (ATLAS) (hereafter, 19Y4), discovered by the Asteroid Terrestrial-impact Last Alert System (ATLAS) at the Mauna Loa Observatory on 2019 December 28, is a long-period comet. According to the JPL orbital solution #17, it takes 19Y4 5895 ± 23 yr to orbit the Sun in an elliptical trajectory of eccentricity $e = 0.999$, inclination $i = 45.4^\circ$, and perihelion distance $q = 0.253$ AU.¹ Its initial light curve exhibited such a steep brightening that, if continued, 19Y4 would have been visible to naked eyes when approaching its perihelion in 2020 late May.² However, the steep brightening terminated in 2020 mid-March, when 19Y4 started to disintegrate, as revealed by the nongravitational effect and a blue color likely caused by the release of a large amount of volatiles ([Hui & Ye 2020](#)). The polarization increased dramatically in 2020 late-March as well, indicating a large increase in the amount of carbonaceous material ([Zubko et al. 2020](#)). On 2020 April 6, [Ye & Zhang \(2020\)](#) and [Steele et al. \(2020\)](#) successively reported an elongated nucleus. On 2020 April 13, the nucleus of 19Y4 had already split into at least five condensations ([Sekanina et al. 2020](#)). Optical spectroscopy on 2020 April 14 and 16 revealed emission bands of CN, C₂, C₃, and NH₂. The C₂/CN and C₃/CN production-rate ratios suggested a “typical” Oort cloud comet under the A’Hearn classification ([Ivanova et al. 2021](#)). Continuing disintegration was reported by [Ye & Hui \(2020\)](#), and the evolution of the fragment clusters was investigated in detail through high angular resolution images obtained with the *Hubble Space Telescope* (HST) on 2020 April 20 and 23 ([Ye et al. 2021](#)).

To explore the properties of the pristine volatiles and dust beneath the refractory crust, we have performed long-slit spectroscopic and broad-band photometric observations of 19Y4 during its disintegration. This paper reports and analyzes the spectroscopic and photometric data and is organized as follows. The observation and data reduction are described in §2 and the results are reported in §3. The gas and dust productions are discussed in §4.1 and §4.2, respectively. The dust-scattered light is modeled in §4.3 to infer the properties of the dust. We summarize our major conclusions in §5.

2. OBSERVATION AND DATA REDUCTION

2.1. Long-slit Spectroscopy

We obtained long-slit optical spectra of 19Y4 with the Beijing Faint Object Spectrograph and Camera (BFOSC) on board the 2.16-Meter Telescope at Xinglong Station. BFOSC has a 2048×2048

¹ https://ssd.jpl.nasa.gov/tools/sbdb_lookup.html#/?sstr=2019Y4

² <http://astro.vanbuitenen.nl/comet/2019Y4>

pixel² CCD installed, subtending a $9.36' \times 9.36'$ field of view (FOV). The pixel scale is thus $\sim 0.274''$ and no binning was performed. The slit length of $9.4'$ was fixed along the north-south orientation. We note that the north-south orientation is parallactic only when the target is on the meridian. So our spectra are somewhat subjected to atmospheric dispersion (see §3). A slit width of $1.8''$ or $2.3''$ was chosen, depending on the seeing at the time of observation. The G4 grism, covering a wavelength range of $3600\text{--}8700 \text{ \AA}$, was used. It has a resolving power of ~ 265 at $[\text{O III}] \lambda 4959 \text{ \AA}$ and $\lambda 5007 \text{ \AA}$, if combined with a slit width of $2.3''$ (Fan et al. 2016).

We performed spectroscopic observations of 19Y4 in four nights: 2020 April 6.51, 13.53, 20.53, and 23.58 (UT). Although the disintegration of the nucleus had already started in mid-March 2020 (Hui & Ye 2020), no fragment was resolved in our observation on April 6.51 (UT), and the slit was centered on the brightest pixels of the elongated nucleus. On April 13.53 (UT), the slit was centered on the fragment 19Y4-A (see Figure 1a). On April 20.53 (UT), fragments 19Y4-A and 19Y4-B were resolved and they roughly aligned along the north-south orientation (see Figure 1b), therefore, the slit was over both of them. On April 23.58 (UT), the slit was centered on the brightest fragment 19Y4-B. Non-sidereal tracking was used. We alternated between short exposures of 600 s and slit view inspections in order to ensure the guiding accuracy. The iron-argon arc was used as the wavelength calibrator. In addition, we have also obtained the long-slit spectra of several flux standards: Feige 34, He 3, HR 4554, HD 109995, HZ 44 and Feige 98. The spectroscopy log is shown in Table 1. Also tabulated in Table 1 are the kinematic parameters of 19Y4, including its phase angle (ϕ), heliocentric (r_h), and geocentric distances (Δ) as well as their temporal changing rates \dot{r}_h and $\dot{\Delta}$, obtained from the JPL Horizons On-Line Ephemeris System web-interface.³

Following the general data reduction procedures, we reduced the long-slit spectroscopic data with Python. First, we took bias subtraction, corrected for flat fields, and removed cosmic rays. Then, we corrected for the geometric curvature by fitting the curved arc lines with the B-spline functions. Finally, we combined multiple short exposures in each night, and calibrated their wavelengths and fluxes to derive fully reduced 2-D spectra.

2.2. Broadband Photometry

BFOSC was also used to perform broadband photometry over 19Y4 on 2020 April 23.55 (UT). The CCD configuration is the same as that used in the long-slit spectroscopy (see §2.1). We made three exposures of 300 s each, with the *BVRI* filters in the Johnson-Cousins system. Again, non-sidereal tracking was used. The photometry log is also shown in Table 1.

We developed a Python pipeline to reduce the photometric data. First, we corrected all the science frames for bias, flat field and cosmic ray pixels. Then, we smoothed the corrected frames to detect and center the peaks of the trailed field stars, which were flattened under non-sidereal tracking. We performed photometry at each centroid on the corrected frames with rectangular aperture and annulus to obtain instrumental magnitudes. Next, we used the centroids of the star trails to derive plate solutions via *Astrometry.net* (Lang et al. 2010), and the instrumental magnitudes to derive flux zeropoints by cross-match with the Sloan Digital Sky Survey Data Release 16 catalog (Ahumada et al. 2022). The *BVRI* fluxes and errors of the field stars were constructed from the Sloan *gri* fluxes and errors according to the transformation relations given in Chonis & Gaskell (2008). The flux calibrated frames were finally combined according to their filters.

³ <https://ssd.jpl.nasa.gov/horizons.cgi>

3. RESULTS

We adopt two apertures, different in width, to extract 1-D spectra: the narrow one, with a single aperture, has a width of $\sim 27.5''$ (corresponding to a physical scale of $\sim 2.4 \times 10^4$ km); the broad one, divided into 40 sub-apertures, has a width $\sim 165''$ in total (corresponding to a physical scale of $\sim 1.2 \times 10^5$ km; see Figure 1). The narrow aperture is chosen to maximize the signal-to-noise ratio in the dust continuum bands, and the extracted spectra are used to determine the reflectivity gradients (see below). We show in Figure 2 the narrow aperture spectra of 19Y4. The spectra are composed of emission bands from gases and sunlight scattered by dust grains. With the help of an emission line catalog (Brown et al. 1996), we identify the $\Delta\nu = 0$ bands of CN, C₂, and C₃, the $\Delta\nu = +1$ band of C₂, and a series of bands of NH₂. The sub-aperture spectra are used to both estimate the influence of atmospheric dispersion on the reflectivity gradients (see below) and model the gas and dust production (see §4.1 and §4.2).

Figure 3 shows the *BVRI* images of 19Y4 obtained with BFOSC on 2020 April 23.55 (UT). As the band goes from *B* to *I*, the coma of 19Y4 shows a less-extended morphology, indicating the broadband colors vary from inner to outer coma. To characterize the color variation, we derive $(B - V)$ and $(V - R)$ profiles of the coma by performing photometry with a slit-like aperture along the north-south orientation. The aperture is divided into a series of sub-apertures, $4.1''$ in height and $2.3''$ in width (see Figure 3), which are the same as that used to extract sub-aperture spectra. The color profiles are shown in Figure 4. In general, the $(B - V)$ profile is slightly redder and the $(V - R)$ profile is significantly bluer than the solar colors of $(B - V)_{\odot} = 0.653 \pm 0.005$ and $(V - R)_{\odot} = 0.352 \pm 0.007$ (Ramírez et al. 2012). More specifically, the $(B - V)$ profile has a local minimum of 0.68 near the nucleus and becomes redder outwards. After reaching ~ 0.9 at $\sim 30''$ from the nucleus, it starts to turn blue. The $(V - R)$ profile has a maximum of -0.07 near the nucleus and becomes bluer outwards. As the broad *BVR* bands cover multiple gas emission lines and dust continuum, such color variation should not be simply attributed to the intrinsic changes in the nature of gas or dust. Instead, it may merely reflect the spread of gases and dust in the coma. To be more quantitative, we estimate from the spectra that the gas emission bands contribute $\sim 50\%$ and $\sim 25\%$ of the *VR* fluxes, respectively. This suggests that the blue color of $(V - R)$ does not necessarily indicate a blue dust continuum of 19Y4.

To characterize the dust color, we define seven dust continuum bands free from gas emission and telluric absorption: 5225–5255 Å, 5800–5850 Å, 6410–6450 Å, 6800–6850 Å, 7420–7450 Å, 7540–7580 Å, 7795–7821 Å, and 8000–8050 Å, and derive the reflectivity gradient, following Jewitt & Meech (1986). Observationally, the reflectivity is defined as

$$S_{\lambda}^{\text{obs}}(r_{\text{h}}) = \frac{F_{\lambda}^{\text{sca}}(r_{\text{h}})}{F_{\lambda}^{\odot}(1 \text{ AU})} \times \left(\frac{r_{\text{h}}}{\text{AU}}\right)^2, \quad (1)$$

where $F_{\lambda}^{\text{sca}}(r_{\text{h}})$ is the dust scattered continuum of 19Y4 at a heliocentric distance of r_{h} ; $F_{\lambda}^{\odot}(1 \text{ AU})$ is the solar flux at $r_{\text{h}} = 1 \text{ AU}$. Here we use the solar reference spectrum from CALSPEC (Bohlin et al. 2014). Since the spectra obtained at different epochs have different dust continuum levels, the reflectivity is further normalized to $\langle S^{\text{obs}} \rangle$, the mean reflectivity in the observed wavelength range. We fit $S_{\lambda}^{\text{obs}}/\langle S^{\text{obs}} \rangle$ with linear functions and determine the reflectivity gradient, defined as the slope of the best-fit.

As shown in Figure 5, the reflectivity gradients are negative at wavelengths 5000–8200 Å for all the four epochs, indicating that 19Y4 is significantly bluer than the Sun for which, by definition, the

reflectivity gradient is 0% per 10^3 \AA . It is also bluer than typical comets for which the reflectivity gradient is $\sim 5\text{--}18\%$ per 10^3 \AA at wavelengths $3500\text{--}6500 \text{ \AA}$ (see [Jewitt & Meech 1986](#)). We note that [Hui & Ye \(2020\)](#) also found that 19Y4 at one point had a color that was much bluer than the Sun. However, as we mentioned in §2.1, the spectra of 19Y4 were affected by atmospheric dispersion and so was the color. Therefore, correction is needed to recover the true reflectivity gradient.

To estimate the influence of atmospheric dispersion on the reflectivity gradient, we further derive spectroscopic ($B - V$) and ($V - R$) profiles on April 23.58 (UT) by convolving the sub-aperture spectra with the transmission functions of the BVR filters, and compare them in Figure 4 with the photometric color profiles on the same date. If the spectra were free from atmospheric dispersion, there should not be any difference between the spectroscopic and photometric color profiles, as the apertures used to derive the color profiles are the same. Nevertheless, as shown in Figure 4, the spectroscopic ($B - V$) and ($V - R$) colors are systematically bluer, indicating the influence of the atmospheric dispersion on the colors. To the first-order approximation, we assume that the color deviation due to the atmospheric dispersion varies linearly with the wavelength, and determine a linear correction function by minimizing the systematic differences in the color profiles. We note that such a correction is only applied to the spectrum obtained on 2020 April 23.58 (UT) and, as shown in Figure 5, the recovered reflectivity gradient is $\sim 5\%$ per 10^3 \AA at wavelengths $5000\text{--}8200 \text{ \AA}$. The results are shown in Figure 5 and will be used to constrain the dust properties in §4.3.

4. DISCUSSION

4.1. Gas Production

The gas production rate and scale length of a given volatile species are derived by modeling the “observed” column density profile, which, for species j at a projected distance ρ , is

$$N_j^{\text{obs}} = \frac{4\pi I_j(\rho)}{g_j}, \quad (2)$$

where $I_j(\rho)$ is the continuum-subtracted radiance of the species measured at ρ and integrated over a bandpass, and g_j is the fluorescence efficiency of the species averaged over the band ([Langland-Shula & Smith 2011](#)). We average N_j^{obs} over the two pairs of the sub-apertures symmetric about the nucleus. In this work, we derive the “observed” column density profiles of CN, C_3 and C_2 through their $\Delta\nu = 0$ bands. The bandpasses and fluorescence efficiencies are taken from [Langland-Shula & Smith \(2011\)](#) except for CN ($\Delta\nu = 0$), the fluorescence efficiency of [Schleicher \(2010\)](#) is adopted for which the Swings effect ([Swings 1941](#)) is taken into account. We show in Figure 6 the “observed” column density profiles of CN, C_3 , and C_2 .

In the literature, cometary gas production rates, scale lengths and their dependencies on r_h have been carefully investigated in numerous statistical works (e.g., see [A’Hearn et al. 1995](#); [Fink & Hicks 1996](#); [Langland-Shula & Smith 2011](#)). We apply those results as prior knowledge for Bayesian inference studies. To this end, we assume a log-uniform prior for the gas production rate Q and normal priors for both primary (l_0) and product (l_1) scale lengths, i.e., $\log Q \sim \mathcal{U}(22, 28)$, $l_0 \sim \mathcal{N}(\hat{l}_0, \hat{\sigma}_{l_0}^2)$ and $l_1 \sim \mathcal{N}(\hat{l}_1, \hat{\sigma}_{l_1}^2)$, where $\hat{l}_0, \hat{\sigma}_{l_0}$ and $\hat{l}_1, \hat{\sigma}_{l_1}$ are taken from [Langland-Shula & Smith \(2011\)](#). Here \mathcal{U} and \mathcal{N} are probability functions. With $\log Q \sim \mathcal{U}(22, 28)$, we assume that the production rate Q is uniformly distributed between 10^{22} s^{-1} and 10^{28} s^{-1} in the log space. As we do not have any knowledge about Q , we should assume such a non-informative prior. l_0 and l_1 are scale lengths for

both of which we assume Gaussian priors, as their values have been well investigated in previous statistical studies. The Gaussian parameters $\hat{l}_0, \hat{\sigma}_{l_0}$ and $\hat{l}_1, \hat{\sigma}_{l_1}$ (i.e., mean and standard deviation) are taken from [Langland-Shula & Smith \(2011\)](#). The use of Bayesian inference is justified later in this section. The corresponding prior probability density function is denoted as $p(Q, l_0, l_1)$. From Bayes' theorem, the posterior density is proportional to the prior multiplied by a likelihood function, i.e.,

$$p(Q, l_0, l_1 | N^{\text{obs}}; \sigma_{N^{\text{obs}}}, \rho) \propto p(N^{\text{obs}} | Q, l_0, l_1; \sigma_{N^{\text{obs}}}, \rho) \times p(Q, l_0, l_1) \quad , \quad (3)$$

where $\sigma_{N^{\text{obs}}}$ is the uncertainty of N^{obs} . If $\sigma_{N^{\text{obs}}}$ is assumed to be Gaussian, the likelihood function can be defined as

$$p(N^{\text{obs}} | Q, l_0, l_1; \sigma_{N^{\text{obs}}}, \rho) = \prod_i \frac{1}{\sqrt{2\pi}\sigma_{N_i^{\text{obs}}}} \exp \left[-\frac{(N_i^{\text{mod}} - N_i^{\text{obs}})^2}{2\sigma_{N_i^{\text{obs}}}^2} \right] \quad , \quad (4)$$

where N_i^{mod} is the modeled column density in the i -th sub-aperture. With a set of (Q, l_0, l_1) given, N_i^{mod} can be derived from eqs. (11)–(13) in [Langland-Shula & Smith \(2011\)](#). The joint posterior distributions are then sampled using the Markov chain Monte Carlo (MCMC) method. The 50% (median) and $50 \pm 34\%$ percentiles in the marginalized distributions of Q, l_0 and l_1 are taken as the best-fit values and the uncertainties, respectively. Note that, in the fitting, N_i^{obs} with $\rho_i < 5 \times 10^3$ km are excluded, considering that the gas distribution in the inner coma may not be spherically symmetric due to the disintegration and also that “holes” may be present in the profiles of C_2 (see [Langland-Shula & Smith 2011](#)).

The best-fits to the “observed” column density profiles are shown in [Figure 6](#), with the best-fit model parameters and uncertainties listed in [Table 2](#). The fits to C_3 ($\Delta\nu = 0$) on 2020 April 6.51 and 23.58 (UT) fail due to the low signal-to-noise ratio of the observational data, and are thus not shown. Typically, to simultaneously determine both l_0 and l_1 , the “observed” profiles are required to extend further than l_1 ([Fray et al. 2005](#)). However, this is not the case here. If the widely adopted χ^2 -minimizing method is used, several (l_0, l_1) pairs could lead to equally good fits ([Fray et al. 2005](#); [Langland-Shula & Smith 2011](#)). Therefore, it is the Bayesian model or, more specifically, the prior that helps to find unique best-fits.

Since G4 does not cover any strong OH bands, we take $Q(\text{CN})$ as an indicator of the gas production rate of 19Y4. We show in [Figure 7a](#) the dependency of $Q(\text{CN})$ on r_h . In general, the gas production rate in 19Y4 is “typical” in the sense that both the production rate and its dependency on r_h agree with that of the 26 comets reported in [Langland-Shula & Smith \(2011\)](#).

We estimate a mean ratio of $\log [Q(C_2)/Q(\text{CN})] \approx 0.2$ and $\log [Q(C_3)/Q(\text{CN})] \approx -1.2$ at $r_h = 1$ AU, if we assume $\log [Q(C_2)/Q(\text{CN})]$ and $\log [Q(C_3)/Q(\text{CN})]$ follow a power-law dependence on r_h and take the power-law slopes of [Langland-Shula & Smith \(2011\)](#). The C_2/CN and C_3/CN production rate ratios estimated for 19Y4 suggest a “typical” comet instead of a “depleted” one under the classification of [A’Hearn et al. \(1995\)](#), consistent with that found by [Ivanova et al. \(2021\)](#).

4.2. Dust Production

Initially introduced in [A’Hearn et al. \(1984\)](#), the so-called $Af\rho$ quantities are often used to describe cometary dust production, where A is the dust reflectivity (i.e., albedo), f is the dust filling factor and ρ is the projected linear radius of the FOV at the comet as discussed in [§4.1](#). The $Af\rho$ quantity within a circular aperture with a projected radius of ρ is determined directly from observation as

$$Af\rho = \frac{(2\Delta)^2}{\rho} \left(\frac{r_h}{\text{AU}} \right)^2 \frac{F_c}{F_\odot(1 \text{ AU})} \frac{1}{\Phi_{\text{HM}}(\phi)} , \quad (5)$$

where F_c is the cometary flux in a chosen dust continuum band, $F_\odot(1 \text{ AU})$ is the solar flux at $r_h = 1 \text{ AU}$ in the same band, and $\Phi_{\text{HM}}(\phi)$ is the normalized Halley-Marcus phase function (Schleicher & Bair 2011). In most cases, F_c is obtained from narrow-band photometry. But it can also be constructed from long-slit spectroscopy by considering a geometric correction function

$$F_c = \sum_i G(\rho_i) F(\rho_i) , \quad (6)$$

where ρ_i is the projection distance from the i -th sub-aperture to the comet nucleus, and $G(\rho_i)$ is the geometric correction function (Langland-Shula & Smith 2011). The summation is over all the sub-apertures within ρ (i.e., $\rho_i < \rho$). In this work, we calculate $Af\rho$ from the constructed F_c in the $\lambda 4850 \text{ \AA}$ and $\lambda 5240 \text{ \AA}$ continuum bands refined in Langland-Shula & Smith (2011) with an aperture radius of 10000 km. The results are tabulated in Table 3. We should admit that our method of reconstructing $Af\rho$ from long-slit spectra which only sample a strip along certain part of the coma has a drawback of not accounting for the coma's asymmetry, even more so for a disintegrating comet. However, detailed analysis of dust production during disintegration requires high resolution, spatially resolved photometry and detailed modeling, which is beyond the scope of this work. Nevertheless, we note that our $Af\rho$ values closely agree with that from narrow-band photometry measured with TRAPPIST (Y. Moulane, private conversation).

We obtain a mean $Af\rho$ for 19Y4 by averaging over that in the $\lambda 4850 \text{ \AA}$ and $\lambda 5240 \text{ \AA}$ continuum bands and examine the dependency of $Af\rho$ on r_h in Figure 7b. For comparison, we also show in Figure 7b the $Af\rho$ quantities of the 26 comets studied in Langland-Shula & Smith (2011). While 19Y4 appears to be less dusty, it exhibits a r_h -dependence more or less resembling that of the Langland-Shula & Smith (2011) samples for which a power-law with an index 5.3 ± 0.6 is suggested, even though most comets in the sample of Langland-Shula & Smith (2011) did not disintegrate when observed.

4.3. Scattered Sunlight

The dust-scattered light observationally determined in §3 can be used to infer the dust size, compositional, and structural properties. To reproduce the normalized reflectivity $S_\lambda^{\text{obs}}/\langle S^{\text{obs}} \rangle$ (see §3 and Figure 8), we adopt the cometary dust model of Li & Greenberg (1998b), which assumes cometary dust grains to be porous aggregates of small astronomical silicates, amorphous carbon, and vacuum. We consider two cases for the porosity (i.e., the fractional volume of vacuum): $f_{\text{vac}} = 0.9$ and $f_{\text{vac}} = 0.5$, which are roughly the upper and lower limits for cometary dust grains (see Greenberg & Hage 1990; Greenberg 1998). For porous dust resulting from coagulative growth, one would expect a porosity higher than $f_{\text{vac}} = 0.5$ (see Blum & Wurm 2008). On the other hand, polarimetric measurements suggest that, for most of the time, amorphous silicates in the coma of 19Y4 account for a fractional volume (f_{sil}) of 0.17–0.28 (Zubko et al. 2020). Therefore, we assume a bulk volume mixing ratio of $f_{\text{carb}}/f_{\text{sil}} = 3$ for our dust model. The refractive indices of amorphous silicates and amorphous carbon are taken, respectively, from Draine & Lee (1984) and Rouleau & Martin (1991).

We use Mie theory combined with the Bruggman effective medium theory (Bohren & Huffman 1983) to calculate $C_{\text{sca}}(\lambda, a)$ and $g(\lambda, a)$, the scattering cross sections and asymmetry factors of spherical porous aggregates of radii a at wavelength λ . Here the aggregate size a refers to the radius of the

sphere encompassing the entire aggregate (we assume that all grains are spherical in shape). We assume a power-law dust size distribution, $dn/da \propto a^{-\alpha}$, over the size range $a_{\min} \leq a \leq a_{\max}$. The model reflectivity, $S^{\text{mod}}(\lambda)$, is calculated as

$$S^{\text{mod}}(\lambda) \propto \int_{a_{\min}}^{a_{\max}} C_{\text{sca}}(\lambda, a) \Phi_{\text{HG}} [g(\lambda, a); \theta] \frac{dn}{da} da \quad , \quad (7)$$

where θ , defined as $\pi - \phi$, is the scattering angle, and $\Phi_{\text{HG}} [g(\lambda, a); \theta]$ is the Henyey-Greenstein phase function (Henyey & Greenstein 1941). Note that the right-hand side differs from the absolute reflectivity by some scaling factor. However, similar to $S^{\text{obs}}(\lambda)$, $S^{\text{mod}}(\lambda)$ is normalized with respect to the averaged value over the defined continuum wavelengths to produce $S_{\lambda}^{\text{mod}} / \langle S^{\text{mod}} \rangle$ during which the scaling factor is cancelled out. It is apparent that the model reflectivity $S^{\text{mod}}(\lambda)$ contains information about the dust size, composition and morphology since the scattering cross section $C_{\text{sca}}(\lambda, a)$ and the asymmetry factor $g(\lambda, a)$ are dependent on the dust size a , composition (through the refractive index), and morphology (e.g., porosity).

We calculate normalized reflectivities with different size distributions. Four size ranges are considered, different in the lower cutoff, i.e., $a_{\min} = 0.1, 1, 10,$ and $100 \mu\text{m}$. The upper cutoff (a_{\max}) is fixed to $1000 \mu\text{m}$. The resulting reflectivity gradient is not sensitive to the choice of a_{\max} since the scattering in the optical by such mm-sized or larger grains is gray (e.g., see Li 2008). Given a size range, we vary α from 2.5 to 4.1, the flattest and the steepest power-law for cometary dust grains from space measurements (McDonnell et al. 1991; Lasue et al. 2009; Price et al. 2010). The parameters are tabulated in Table 4.

We compare the model reflectivities in Figure 8 with the reflectivity derived from observations in §3. Models with same a_{\min} but different α are grouped and shown as shadows of different colors. Figure 8 shows that the “observed” reflectivity gradient (i.e., 5% per 10^3 \AA) can be explained by different combinations of dust parameters. For highly porous dust with $f_{\text{vac}} = 0.9$, models with $a_{\min} = 1 \mu\text{m}$ and $a_{\min} = 10 \mu\text{m}$ are able to reproduce the “observed” reflectivity gradient. For dust with a lower porosity of $f_{\text{vac}} = 0.5$, while models with $a_{\min} = 10 \mu\text{m}$ result in reflectivity gradients too flat to be comparable with observed, the “observed” reflectivity gradient can be reproduced by dust with $a_{\min} = 1 \mu\text{m}$. Apparently, although the limited observational constraint does not allow us to uniquely determine the dust parameters, the porous dust model is capable of accounting for the “observed” reflectivity gradient with appropriate combination of parameters. In general, the reflectivity gradient $S^{\text{mod}}(\lambda)$ decreases as the dust becomes more porous or a_{\min} becomes smaller. The variation of $S^{\text{mod}}(\lambda)$ with α , the power index of the dust size distribution, depends on the choice of a_{\min} . For $a_{\min} < 1 \mu\text{m}$, $S^{\text{mod}}(\lambda)$ becomes bluer as α increases, due to the increasing role played by submicron-sized grains which scatter more at shorter wavelengths. By increasing a_{\min} to several microns (and larger), $S^{\text{mod}}(\lambda)$ becomes redder as α increases since these micron-sized grains scatter more effectively at longer wavelengths. With a_{\min} reaching several tens of microns, $S^{\text{mod}}(\lambda)$ becomes gray and does not vary with α since these grains are in the geometrical optics limit and their scattering does not vary much with wavelength. Apparently, a_{\min} plays a more important role than α in determining $S^{\text{mod}}(\lambda)$.

5. SUMMARY

We presented long-slit optical spectra at $\sim 3600\text{--}8700\text{ \AA}$ and multi-band *BVRI* images of the disintegrating comet 19Y4, from which we derived the gas and dust production rates and modeled the dust-scattering reflectivity. Our principal results are as follows:

1. All of the spectra taken during the disintegration showed strong gas emission. The production rates of CN, C₂, and C₃ and the corresponding C₂/CN and C₃/CN production-rate ratios were derived. Both the gas production rates and their dependencies on r_h are consistent with that of “typical” Oort cloud comets, not that of carbon-chain “depleted” Kuiper Belt comets.
2. The dust-scattering reflectivity of 19Y4 was somewhat red, with a gradient of $\sim 5\%$ per 10^3 \AA . The reflectivity gradient was modeled in terms of porous dust. The red color is accounted for by porous dust.

ACKNOWLEDGMENTS

We thank the anonymous referees for their valuable comments and suggestions which improved the quality and presentation of this work. RNZ thanks Dan Yu for her love and companionship over the past eight years, and dedicates this article to their marriage. We acknowledge the support of the staff of the Xinglong 2.16m telescope. This work was partially Supported by the Open Project Program of the CAS Key Laboratory of Optical Astronomy, National Astronomical Observatories, Chinese Academy of Sciences. RNZ and JFL are supported by NSFC through grant numbers 11988101 and 11933004. LW is supported by NSFC through grant number U2031144. JFL acknowledges the support from the New Cornerstone Science Foundation through the New Cornerstone Investigator Program and the XPLOER PRIZE.

Facilities: Beijing:2.16m (BFOSC)

Software: *astropy* (Astropy Collaboration et al. 2013), *ccdproc* (Bardyn et al. 2017), *photutils* (Bradley et al. 2019), *astroquery* (Ginsburg et al. 2019), *specutils* (Astropy-Specutils Development Team 2019), *sbpy* (Mommert et al. 2019), *lmfit* (Newville et al. 2014), *emcee* (Foreman-Mackey et al. 2013),

REFERENCES

- | | |
|--|---|
| <p>A’Hearn, M. F., Millis, R. C., Schleicher, D. O.,
Osip, D. J., & Birch, P. V. 1995, <i>Icarus</i>, 118,
223, doi: 10.1006/icar.1995.1190</p> | <p>A’Hearn, M. F., Schleicher, D. G., Millis, R. L.,
Feldman, P. D., & Thompson, D. T. 1984, <i>AJ</i>,
89, 579, doi: 10.1086/113552</p> |
|--|---|

Table 1. Log of BFOSC observations.

Date of 2020 (UT)	Object	Grism/Filter	Slit Width ($''$)	Exposure (s)	Airmass	r_h^a (AU)	r_h (km s^{-1})	Δ^b (AU)	$\dot{\Delta}$ (km s^{-1})	ϕ^c ($^\circ$)
Apr. 6.51	19Y4	G4	1.8	6×600	1.215	1.37	-32.4	1.03	-5.55	46.6
Apr. 6.54	Feige 34			600	1.012					
Apr. 13.53	19Y4	G4	2.3	6×600	1.279	1.24	-33.7	1.00	-6.03	51.8
Apr. 13.56	He 3			600	1.389					
Apr. 20.53	19Y4	G4	2.3	4×600	1.404	1.10	-35.4	0.98	-7.33	57.2
Apr. 20.56	HR 4554			5	1.037					
Apr. 20.59	HD 109995			120	1.014					
Apr. 23.55	19Y4	<i>BVRI</i>		3×300	1.526	1.04	-36.1	0.97	-8.10	59.9
Apr. 23.58	19Y4	G4	1.8	1×600	1.763	1.04	-36.1	0.97	-8.10	59.9
Apr. 23.59	HD 109995			30	1.005					
Apr. 23.67	HZ 44			360	1.012					
Apr. 23.84	Feige 98			600	1.412					

^aHeliocentric distance^bGeocentric distance^cPhase angle**Table 2.** Gas production rates and scale lengths.^a

Date of 2020 (UT)	r_h (AU)	CN			C ₃			C ₂			Ref. ^b
		Q (10^{25} s^{-1})	l_0 (10^4 km)	l_1 (10^4 km)	Q (10^{25} s^{-1})	l_0 (10^4 km)	l_1 (10^4 km)	Q (10^{25} s^{-1})	l_0 (10^4 km)	l_1 (10^4 km)	
Apr. 6.51	1.37	$4.4^{+0.3}_{-0.3}$	$6.5^{+0.5}_{-0.5}$	38^{+6}_{-6}	—	—	—	$3.5^{+0.4}_{-0.4}$	$5.7^{+0.7}_{-0.6}$	13^{+3}_{-2}	1
Apr. 13.53	1.24	$3.7^{+0.2}_{-0.2}$	$3.5^{+0.2}_{-0.2}$	35^{+8}_{-6}	$0.21^{+0.01}_{-0.01}$	$1.0^{+0.1}_{-0.1}$	27^{+5}_{-4}	$4.1^{+0.1}_{-0.2}$	$7.3^{+0.2}_{-0.3}$	$8.0^{+0.3}_{-0.2}$	1
Apr. 14.74	1.21	<1.05	3.2	43	<0.015	0.15	8.8	<0.83	2.4	16	2
Apr. 16.77	1.17	<1.12	3.0	41	<0.015	0.14	8.2	<0.79	2.2	15	2
Apr. 20.53	1.10	$1.8^{+0.3}_{-0.3}$	$3.2^{+0.6}_{-0.5}$	8^{+2}_{-2}	$0.11^{+0.01}_{-0.01}$	$1.3^{+0.1}_{-0.1}$	16^{+4}_{-3}	$3.4^{+0.1}_{-0.2}$	$7.2^{+0.3}_{-0.3}$	$8.7^{+0.5}_{-0.4}$	1
Apr. 23.58	1.04	$1.3^{+0.1}_{-0.1}$	$4.1^{+0.3}_{-0.3}$	30^{+6}_{-5}	—	—	—	$1.5^{+0.1}_{-0.1}$	$5.6^{+0.5}_{-0.4}$	10^{+1}_{-1}	1

^aThe production rates of [Ivanova et al. \(2021\)](#) were merely upper limits. Also, when [Ivanova et al. \(2021\)](#) derived the production rates from the Haser model, they adopted a set of scale lengths which are different from ours. Note that our rates are consistent with that derived from the TRAPPIST observations (Y. Moulane, private conversation).

^bReference: (1) This work; (2) [Ivanova et al. \(2021\)](#)

Table 3. $Af\rho$ within $\rho = 10000$ km in $\lambda 4850 \text{ \AA}$ and $\lambda 5240 \text{ \AA}$ bands.

Date of 2020 (UT)	r_h (AU)	$Af\rho$	
		$\lambda 4850 \text{ \AA}$ (cm)	$\lambda 5240 \text{ \AA}$ (cm)
Apr. 6.51	1.37	972 ± 10	753 ± 9
Apr. 13.53	1.24	288 ± 1	199 ± 1
Apr. 20.53	1.10	155 ± 2	97 ± 1
Apr. 23.58	1.04	145 ± 3	73 ± 3

Table 4. Dust model parameters.

f_{vac}	$f_{\text{carb}} / f_{\text{sil}}$	a_{min} (μm)	a_{max} (μm)	α
		0.1		
0.5	3	1	1000	2.5-4.1
		10		
		0.1		
0.9	3	1	1000	2.5-4.1
		10		
		100		

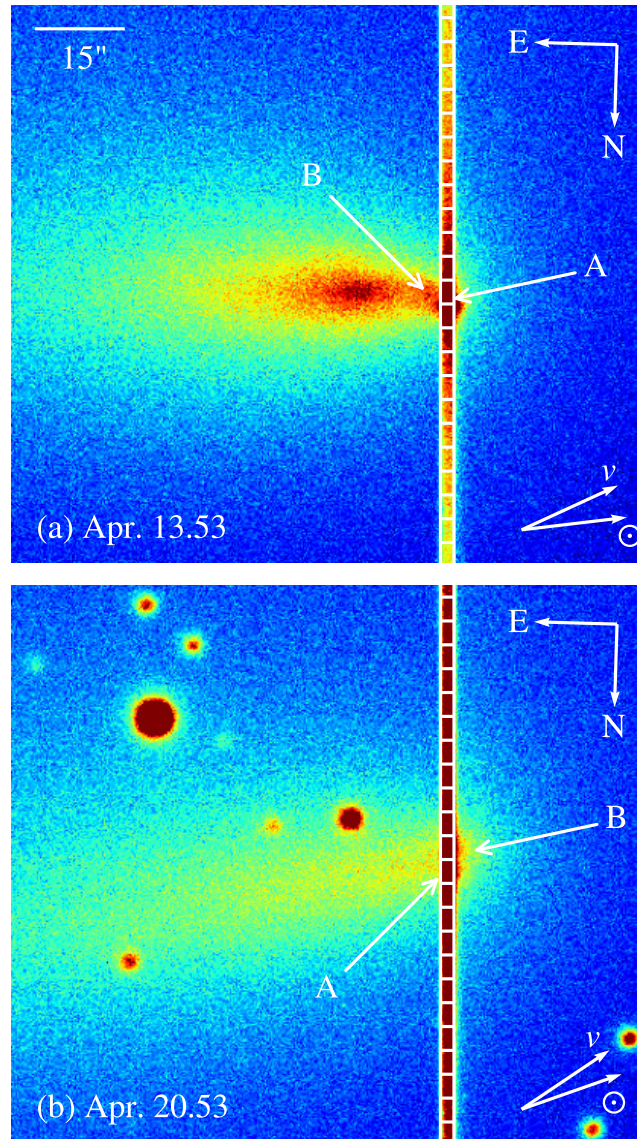


Figure 1. Slit views of C/2019 Y4 (ATLAS) on 2020 April 13.53 and 20.53 (UT). The ephemeris positions of the two major fragments A and B (from MPEC 2020-L06 and 2023-J29, respectively) are marked. On April 13.53 (UT), the slit was centered on A. On April 20.53 (UT), the slit was over both A and B. The rectangles, 4.1'' in height and 2.3'' in width, along the slits are sub-apertures. They were used to extract sub-aperture spectra (see §3). The arrows in the upper right corner mark the north and the east directions, and those in the lower right corners mark the velocity and comet-Sun vectors.

Ahumada, R., Allende Prieto, C., Almeida, A., & et al. 2022, *VizieR Online Data Catalog*, V/154
 Astropy Collaboration, Robitaille, T. P., Tollerud, E. J., et al. 2013, *A&A*, 558, A33, doi: [10.1051/0004-6361/201322068](https://doi.org/10.1051/0004-6361/201322068)
 Astropy-Specutils Development Team. 2019, *Specutils: Spectroscopic analysis and reduction*, *Astrophysics Source Code Library*, record ascl:1902.012. <http://ascl.net/1902.012>

Bardyn, A., Baklouti, D., Cottin, H., et al. 2017, *MNRAS*, 469, S712, doi: [10.1093/mnras/stx2640](https://doi.org/10.1093/mnras/stx2640)
 Blum, J., & Wurm, G. 2008, *ARA&A*, 46, 21, doi: [10.1146/annurev.astro.46.060407.145152](https://doi.org/10.1146/annurev.astro.46.060407.145152)
 Bohlin, R. C., Gordon, K. D., & Tremblay, P. E. 2014, *PASP*, 126, 711, doi: [10.1086/677655](https://doi.org/10.1086/677655)
 Bohren, C. F., & Huffman, D. R. 1983, *Absorption and scattering of light by small particles*

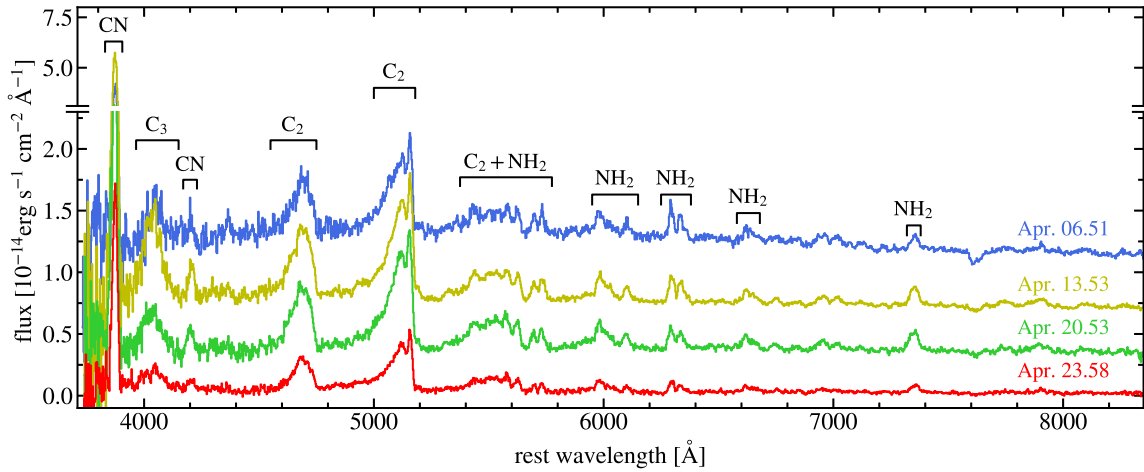


Figure 2. Narrow-aperture BFOSC spectra of C/2019 Y4 (ATLAS) obtained on 2020 April 6.51 (blue line), April 13.53 (yellow line), April 20.53 (green line), and April 23.58 (UT; red line). For comparison, the spectra are vertically shifted by some constants. Strong emission bands are marked.

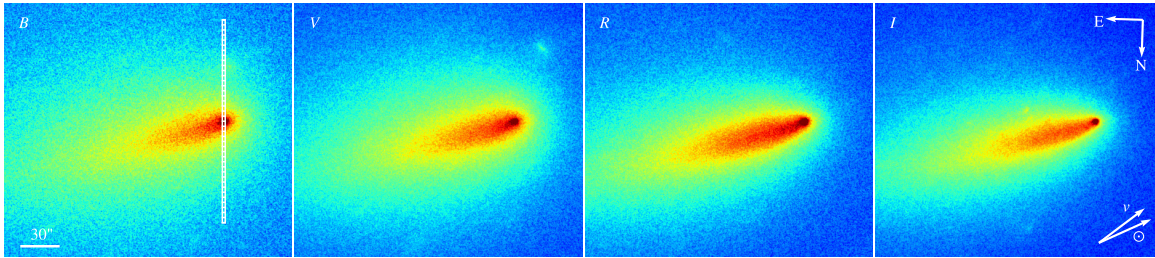


Figure 3. *BVRI* images of C/2019 Y4 (ATLAS) on 2020 April 23.55 (UT). The coma shows a less-extended morphology from *B* to *I*, indicating the broadband colors vary from inner to outer coma. The white rectangle is a slit-like aperture. It is divided into a series of sub-apertures, 4.1'' in height and 2.3'' in width, to derive (*B* – *V*) and (*V* – *R*) profiles (see §3). The arrows in the upper right corner mark the north and the east directions, and those in the lower right corners mark the velocity and comet-Sun vectors.

Bradley, L., Sipőcz, B., Robitaille, T., et al. 2019, *astropy/photutils*: v0.6,

doi: [10.5281/zenodo.2533376](https://doi.org/10.5281/zenodo.2533376)

Brown, M. E., Bouchez, A. H., Spinrad, A. H., & Johns-Krull, C. M. 1996, *AJ*, 112, 1197,

doi: [10.1086/118090](https://doi.org/10.1086/118090)

Chonis, T. S., & Gaskell, C. M. 2008, *AJ*, 135, 264, doi: [10.1088/0004-6256/135/1/264](https://doi.org/10.1088/0004-6256/135/1/264)

Draine, B. T., & Lee, H. M. 1984, *ApJ*, 285, 89, doi: [10.1086/162480](https://doi.org/10.1086/162480)

Fan, Z., Wang, H., Jiang, X., et al. 2016, *PASP*, 128, 115005,

doi: [10.1088/1538-3873/128/969/115005](https://doi.org/10.1088/1538-3873/128/969/115005)

Fink, U., & Hicks, M. D. 1996, *ApJ*, 459, 729,

doi: [10.1086/176938](https://doi.org/10.1086/176938)

Foreman-Mackey, D., Hogg, D. W., Lang, D., & Goodman, J. 2013, *PASP*, 125, 306,

doi: [10.1086/670067](https://doi.org/10.1086/670067)

Fray, N., Bénilan, Y., Cottin, H., Gazeau, M. C., & Crovisier, J. 2005, *Planet. Space Sci.*, 53, 1243, doi: [10.1016/j.pss.2005.06.005](https://doi.org/10.1016/j.pss.2005.06.005)

Ginsburg, A., Sipőcz, B. M., Brasseur, C. E., et al. 2019, *AJ*, 157, 98,

doi: [10.3847/1538-3881/aafc33](https://doi.org/10.3847/1538-3881/aafc33)

Greenberg, J. M. 1998, *A&A*, 330, 375

Greenberg, J. M., & Hage, J. I. 1990, *ApJ*, 361, 260, doi: [10.1086/169191](https://doi.org/10.1086/169191)

Heney, L. G., & Greenstein, J. L. 1941, *ApJ*, 93, 70, doi: [10.1086/144246](https://doi.org/10.1086/144246)

Hui, M.-T., & Ye, Q.-Z. 2020, *AJ*, 160, 91,

doi: [10.3847/1538-3881/ab9d81](https://doi.org/10.3847/1538-3881/ab9d81)

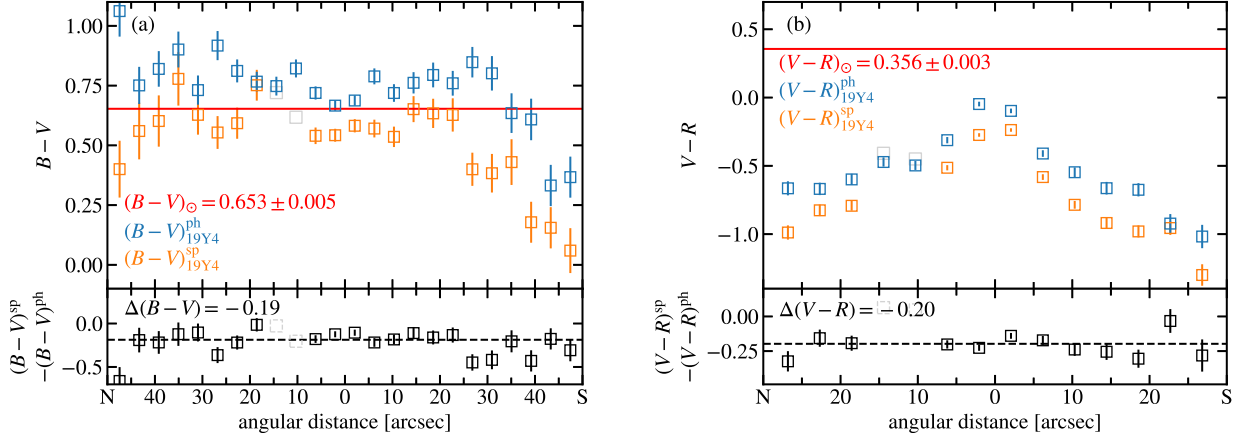


Figure 4. Comparison of the $(B - V)$ (left panel) and $(V - R)$ (right panel) profiles of C/2019 Y4 (ATLAS) derived from photometry (blue open squares) and spectroscopy (yellow open squares), both on 2020 April 23 (UT). Small sections of the spectroscopic profiles are contaminated by field stars (grey open squares). Also shown are the solar colors (red lines). The spectroscopic profiles systematically deviate from the photometric profiles by -0.19 and -0.20 in $(B - V)$ and $(V - R)$, respectively, which are shown as black open squares with fitted black dashed lines. Note that the error bars only account for the propagated Poisson errors. The omitted systematic errors can be approximated by the standard deviations of $\Delta(B - V)$ and $\Delta(V - R)$, which are ~ 0.15 and 0.08 mag, respectively.

Ivanova, O., Luk'yanyk, I., Tomko, D., & Moiseev, A. 2021, *MNRAS*, 507, 5376,

doi: [10.1093/mnras/stab2306](https://doi.org/10.1093/mnras/stab2306)

Jewitt, D., & Meech, K. J. 1986, *ApJ*, 310, 937,

doi: [10.1086/164745](https://doi.org/10.1086/164745)

Lang, D., Hogg, D. W., Mierle, K., Blanton, M., & Roweis, S. 2010, *AJ*, 139, 1782,

doi: [10.1088/0004-6256/139/5/1782](https://doi.org/10.1088/0004-6256/139/5/1782)

Langland-Shula, L. E., & Smith, G. H. 2011, *Icarus*, 213, 280,

doi: [10.1016/j.icarus.2011.02.007](https://doi.org/10.1016/j.icarus.2011.02.007)

Lasue, J., Levasseur-Regourd, A. C., Hadamcik, E., & Alcouffe, G. 2009, *Icarus*, 199, 129,

doi: [10.1016/j.icarus.2008.09.008](https://doi.org/10.1016/j.icarus.2008.09.008)

Li, A. 2008, in *Small bodies in planetary systems* (Berlin: Springer), 167–188

Li, A., & Greenberg, J. M. 1998a, *A&A*, 338, 364

—, 1998b, *ApJL*, 498, L83, doi: [10.1086/311308](https://doi.org/10.1086/311308)

McDonnell, J. A. M., Lamy, P. L., & Pankiewicz, G. S. 1991, *Physical Properties of Cometary Dust*, ed. J. Newburn, R. L., M. Neugebauer, & J. Rahe, Vol. 167, 1043

Mommert, M., Kelley, M., de Val-Borro, M., et al. 2019, *The Journal of Open Source Software*, 4, 1426, doi: [10.21105/joss.01426](https://doi.org/10.21105/joss.01426)

Newville, M., Stensitzki, T., Allen, D. B., &

Ingargiola, A. 2014, *LMFIT: Non-Linear Least-Square Minimization and Curve-Fitting for Python*, 0.8.0, Zenodo,

doi: [10.5281/zenodo.11813](https://doi.org/10.5281/zenodo.11813)

Price, M. C., Kearsley, A. T., Burchell, M. J., et al. 2010, *Meteoritics and Planetary Science*, 45, 1409, doi: [10.1111/j.1945-5100.2010.01104.x](https://doi.org/10.1111/j.1945-5100.2010.01104.x)

Ramírez, I., Michel, R., Sefako, R., et al. 2012, *ApJ*, 752, 5, doi: [10.1088/0004-637X/752/1/5](https://doi.org/10.1088/0004-637X/752/1/5)

Rouleau, F., & Martin, P. G. 1991, *ApJ*, 377, 526, doi: [10.1086/170382](https://doi.org/10.1086/170382)

Schleicher, D. G. 2010, *AJ*, 140, 973,

doi: [10.1088/0004-6256/140/4/973](https://doi.org/10.1088/0004-6256/140/4/973)

Schleicher, D. G., & Bair, A. N. 2011, *AJ*, 141, 177, doi: [10.1088/0004-6256/141/6/177](https://doi.org/10.1088/0004-6256/141/6/177)

Sekanina, Z., Guido, E., & Bryssinck, E. 2020, *Central Bureau Electronic Telegrams*, 4751, 1

Steele, I. A., Smith, R. J., & Marchant, J. 2020, *The Astronomer's Telegram*, 13622, 1

Strazzulla, G. 1999, *SSRv*, 90, 269,

doi: [10.1023/A:1005270703284](https://doi.org/10.1023/A:1005270703284)

Swings, P. 1941, *Lick Observatory Bulletin*, 508, 131, doi: [10.5479/ADS/bib/1941LicOB.19.131S](https://doi.org/10.5479/ADS/bib/1941LicOB.19.131S)

Ye, Q., & Hui, M.-T. 2020, *The Astronomer's Telegram*, 13651, 1

Ye, Q., & Zhang, Q. 2020, *The Astronomer's Telegram*, 13620, 1

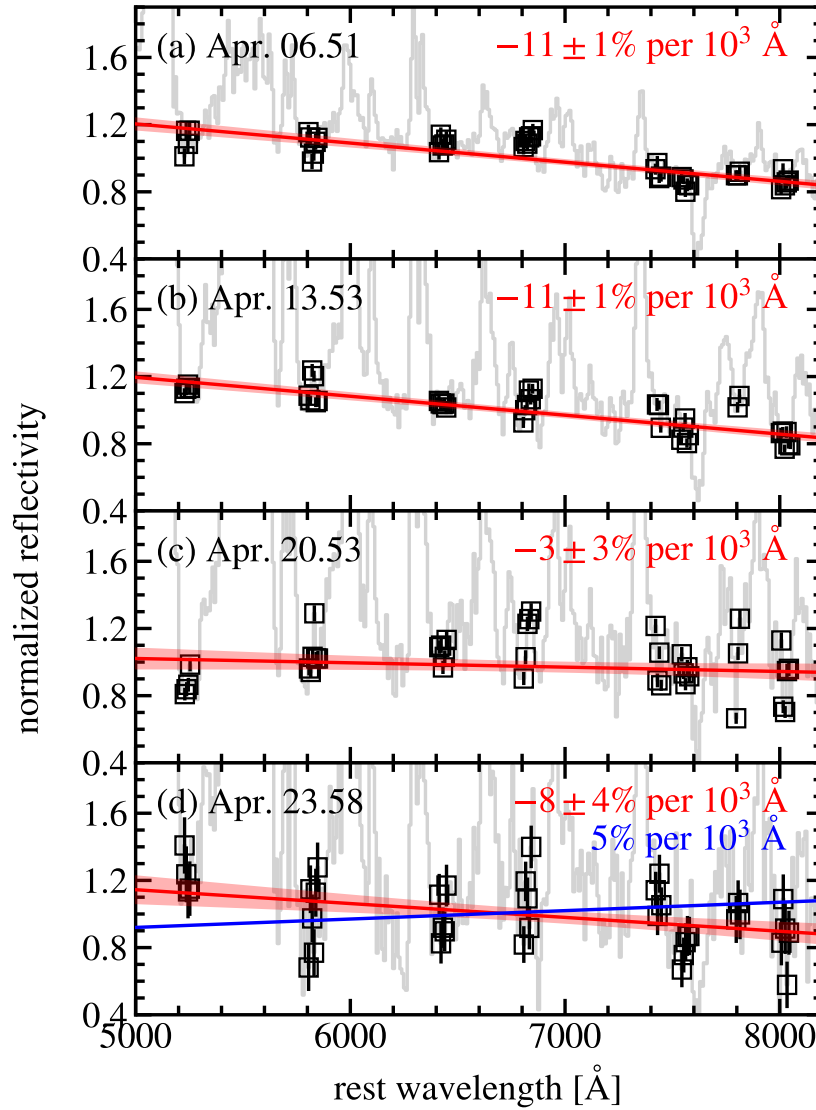


Figure 5. The “observed” reflectivities ($S_{\lambda}^{\text{obs}}/\langle S^{\text{obs}} \rangle$; gray lines) of C/2019 Y4 (ATLAS) on 2020 April 6.51 (a), 13.53 (b), 20.53 (c), and 23.58 (UT; d). The gradients are determined by fitting those in the dust continuum bands (black open squares with error bars) with linear functions (red lines with light red shadows representing the fitting uncertainties). As the spectra of C/2019 Y4 (ATLAS) are somewhat subjected to atmospheric dispersion, the gradients need correction. To the first-order approximation, the reflectivity gradient on April 23.58 (UT) is corrected to $\sim 5\%$ per 10^3\AA (blue line; see §3 for details). All quantities are normalized to their mean values in the observed wavelength range.

Ye, Q., Jewitt, D., Hui, M.-T., et al. 2021, AJ, 162, 70, doi: [10.3847/1538-3881/abfec3](https://doi.org/10.3847/1538-3881/abfec3)

Zubko, E., Zheltobryukhov, M., Chornaya, E., et al. 2020, MNRAS, 497, 1536, doi: [10.1093/mnras/staa1725](https://doi.org/10.1093/mnras/staa1725)

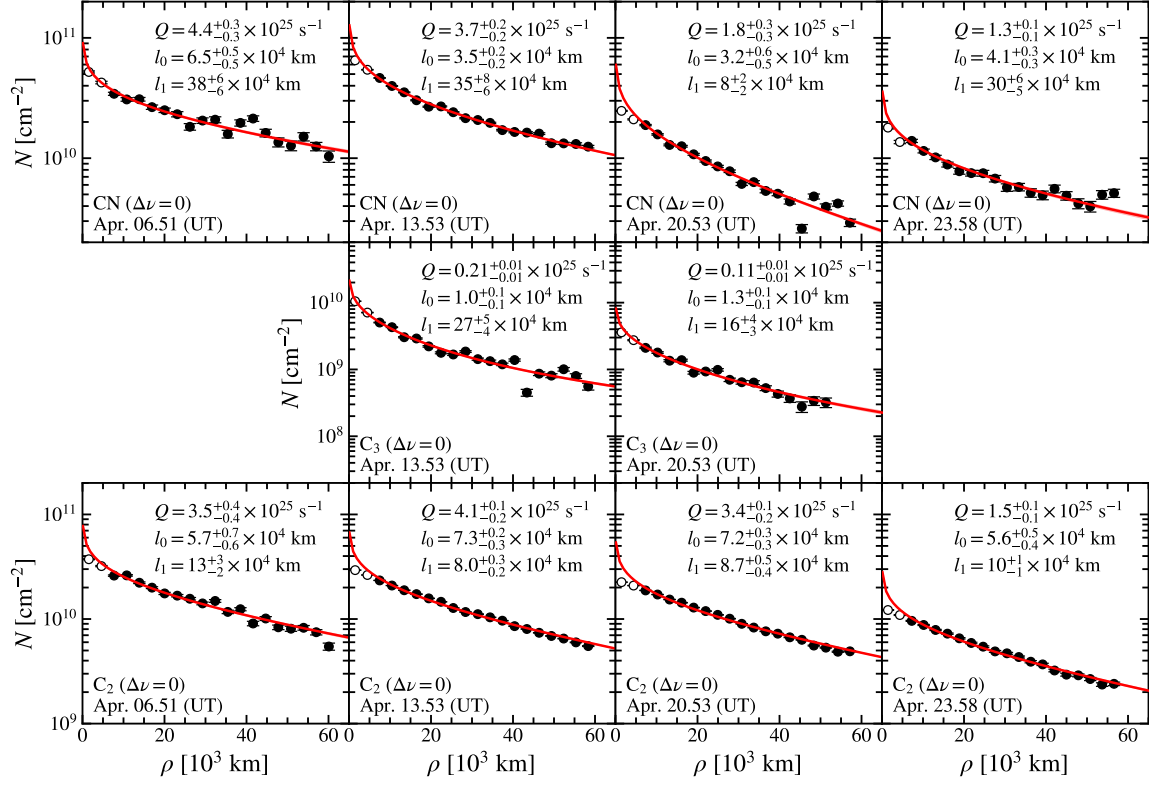


Figure 6. Comparison of the “observed” column density profiles (filled black circles with error bars) of CN ($\Delta\nu = 0$; upper panels), C_3 ($\Delta\nu = 0$; middle panels), and C_2 ($\Delta\nu = 0$; bottom panels) with model fits (solid red lines with light red shadows representing the model uncertainties). In each panel the model parameters are labelled. The open black circles are not considered for modeling (see §4.1 for details).

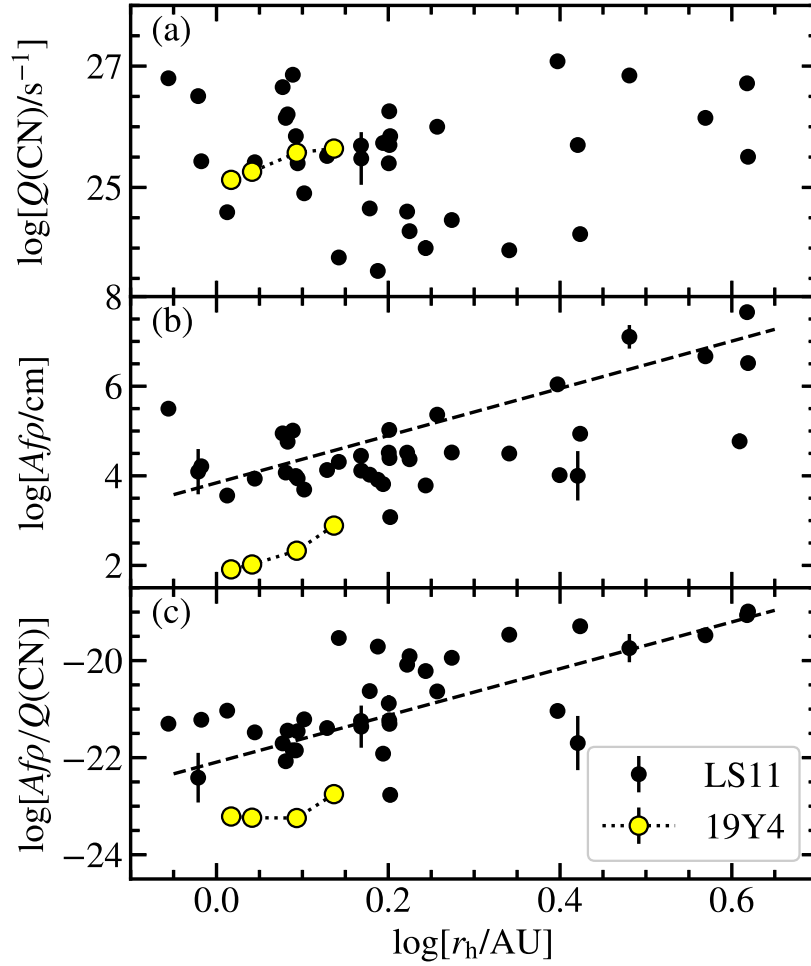


Figure 7. Top panel (a): Variation of the CN production rate $Q(\text{CN})$ of C/2019 Y4 (ATLAS) (yellow circles) with heliocentric distance r_h . Also shown are the CN production rates of the Langland-Shula & Smith (2011) sample of 26 comets (black circles). Middle panel (b): Same as (a) but for $Af\rho$. Also shown is a linear fit to the r_h -dependence of $Af\rho$ for the Langland-Shula & Smith (2011) sample: $d(\log Af\rho)/d(r_h) = 5.3 \pm 0.6$ (black dashed line). Bottom panel: Same as (a) but for $Af\rho/Q(\text{CN})$. The power-law has an index of 4.6 ± 0.8 .

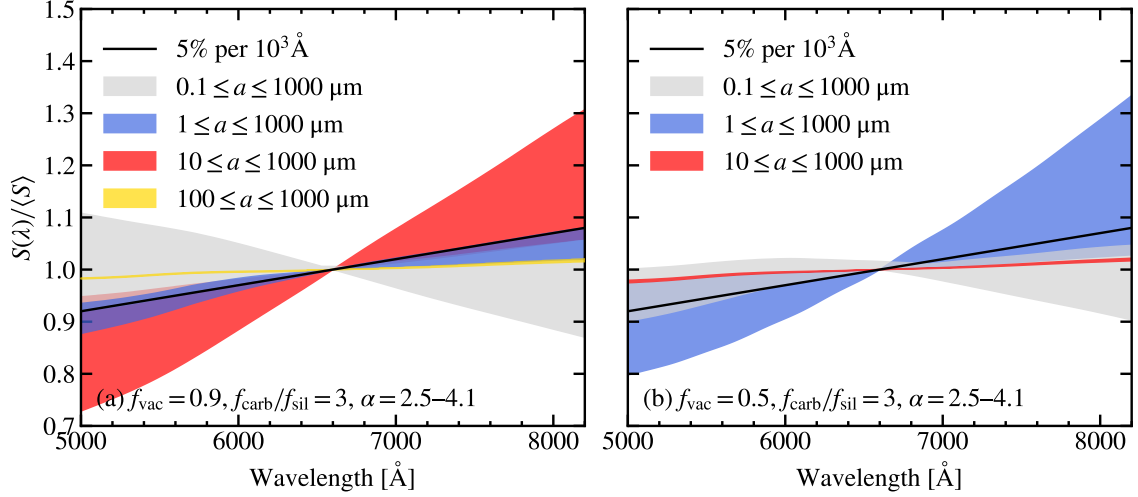


Figure 8. Comparison of the dust models with the recovered reflectivity gradient (black line). For the dust, two cases are considered for the porosity (i.e., the fractional volume of vacuum): $f_{\text{vac}} = 0.9$ (left panel) and $f_{\text{vac}} = 0.5$ (right panel). The volume mixing ratio of amorphous silicate and amorphous carbon is fixed to $f_{\text{carb}}/f_{\text{sil}} = 3$. For the size distribution, four size ranges are considered, different in the lower cutoff, i.e., $a_{\text{min}} = 0.1$ (gray shadow), 1 (blue shadow), 10 (red shadow), and $100 \mu\text{m}$ (yellow shadow). The upper cutoff (a_{max}) is fixed to $1000 \mu\text{m}$. Given a size range, the power-law index α is varied from 2.5 to 4.1. The recovered reflectivity gradient ($\sim 5\%$ per 10^3 \AA) is barely explained by both $1 \leq a \leq 1000 \mu\text{m}$ and $10 \leq a \leq 1000 \mu\text{m}$ when $f_{\text{vac}} = 0.9$, while well explained by the size range $1 \leq a \leq 1000 \mu\text{m}$ when $f_{\text{vac}} = 0.5$. For both cases, larger or smaller a_{min} leads to flatter gradient (or “gray” in color).